PRODUCTION, STRUCTURE, PROPERTIES

Structural Features and Physico-Mechanical Properties of AlN−TiB₂−TiSi₂ Amorphous-Like Coatings

A. D. Pogrebnjak[a, *], **A. A. Demianenko**[a], **A. V. Pshik**[a], **Yu. A. Kravchenko**[a], **O. V. Sobol'**[b], **V. M. Beresnev**[c], **H. Amekura**[d], **K. Kono**[d], **K. Oyoshi**[d], **Y. Takeda**[d], and **I. A. Podchernyaeva**[e]

[a]*Sumy State University, ul. Rimskogo-Korsakova 2, Sumy, 40007 Ukraine*

[b]*Khar'kovskii Polytechnic Institute National Technical University,*
ul. Frunze 21, Khar'kov, 61002 Ukraine

[c]*Karazin Khar'kov National University,*
pl. Svobody 4, Khar'kov, 61022 Ukraine

[d]*National Institute for Materials Science (NIMS),*
1 Chome-2-1 Sengen, Tsukuba, Ibaraki Prefecture 305-0047, Japan

[e]*Frantsevich Institute for Materials Science Problems,*
National Academy of Sciences of Ukraine,
vul. Krzhizhanovs'kogo 3, Kiev, 03680 Ukraine

*e-mail: alexp@i.ua

Received July 9, 2014

Abstract—The coating of the AlN−TiB₂−TiSi₂ system has been produced by the magnetron sputtering of a target. At the high-temperature (900 and 1300°C) actions the coating crystallization to form crystallites of sizes 11−25 nm has been observed. It has been defined that the amorphous-like structure is promising for the use of these coatings as diffusion barriers both as the independent elements and a contacting layer in multilayer wear-resistant coatings. It has been shown that the use of the resultant composite as an effective protective coating for cutting tools will make it possible to increase the tools wear resistance by more than 30% at the temperature up to 1300°C in the cutting zone.

I. INTRODUCTION

The tendencies for permanent increasing the requirements to the efficiency (speed of machining) and quality of the parts of mechanisms together with the established ecological standards determine high demands on the coatings materials. In particular, the requirements for high hardness and high resistance to oxidation [1, 2].

Traditional nitride coatings based on transition metals, like TiN, play an important role in the protection of working surfaces of cutting tools. However, these coatings are characteristic of certain disadvantages; the most important of which is the insufficient resistance to oxidation at high temperatures [3]. The properties of TiN coating may be considerably improved by alloying elements like Al or Si. The addition of Al to the fcc TiN results in the formation of TiAlN coatings, which are characterized by high (~ 32 GPa) hardness [4] and a high (up to 800°C) resistance to oxidation [3], i.e., alloying the coating material by Si ions increases its abilities to resist to the abrasive wear and sputtering by ions of metals [3−5].

The TiSiN nanocomposite coating is the most-studied. Its structure is represented by an amorphous matrix of silicon nitride with imbedded into it TiN nanocrystalls. This coating is characterized by hardness > 40 GPa, high resistance to oxidation (850°C) and high thermostability (up to 1100°C) [6−8]. Later a TiAlSiN fourcomponent nanocomposite coating was produced and studied. Its structure was also presented by amorphous Si_3N_4 and crystalline $Ti_{1−x}Al_xN$ [9−11].

As compared with one-layer coatings, nanolayer coatings that consist of several layers of various materials with nanosize thickness exhibit higher hardness and toughness. Now a great number of such nanolayer coatings, e.g., TiN/SiN_x[12], $TiAlSin/Si_3N_4$ [13], $TiCrN/AlSinN$ [14], $TiAlCrN/AlSin$ [15], $TiN/Cr/Al_2O_3$ [16] have been developed. It was found that their properties depend largely on the thickness of separate layers, numbers and width of interfaces [12−16].

The combination of relatively plastic TiAlN layers with more rigid TiAlSin layers into TiAlSiN nanolayer coatings made it possible to improve properties of a composite by ensuring a considerable increase of hardness, high resistance to oxidation, and thermostability. These coatings have found an efficient application in tools used for high-speed milling of hardened materials without cooling [17].

Recently a tendency has been observed toward the development of coatings having compositions of five and more elements, whose proper combination defines unique advantages of these coatings over coatings with lower numbers of components [18]. The addition of $TiSi_2$ to an $AlN-TiB_2$ composite allows us to produce an $AlN-TiB_2-TiSi_2$ coating, which is expected to have such a complex of properties (due to the formation of an amorphous-like structure), which will make it promising in the use as diffusion barriers both as independent elements and a contacting layer in multilayer wear-resistant coatings [19].

The aim of the present study was to comprehensively investigate the structure, phase composition, surface morphology, and physico-mechanical characteristics of the coating produced by a pulse magnetron sputtering from an $AlN-TiB_2-TiSi_2$ multicomponent target having a low conductivity as well as of variations of the coating properties as a result of a high-temperature action.

2. EXPERIMENTAL

The coating was deposited onto polished samples of molybdenum and grade 45 steel in a plant, whose scheme is described in [19], using a pulse magnetron sputtering of a target. The evaporating materials were $AlN-TiB_2$ with $TiSi_2$ addition high-temperature composite systems developed in the Frantsevich Institute for Materials Problems, National Academy of Sciences of Ukraine. Argon was used as a reaction gas. The regimes of deposition and subsequent machining are shown in Table 1.

Table 1. Parameters of deposition and annealing of $AlN-TiB_2-TiSi_2$ coatings

Series	U_{puls}, V	I, A	U_{displ}, V	Conditions of machining of the coatings produced
1	700	2	200	Was not machined
2	700	2	200	Heating to 200°C for 15 min, heating to 900°C for the following 60 min, holding time ~ 60 min, cooling to 0°C for 30 min
3	700	2	200	Heating to 200°C for 15 min, heating to 1300°C for the subsequent 90 min, holding time ~ 60 min, cooling to 0°C at uncontrolled cooling
4	700	2	200	Heating to 200°C for 15 min, heating to 1300°C for the subsequent 90 min, holding time ~ 60 min, cooling to 0°C (uncontrolled cooling), implantation by Au^- ions with a dose of 1×10^{17} ion/cm^2

Notes: U_{puls} is the pulse voltage, supplied to the target sputtered; U_{disp} is the displacement potential on a substrate.

Morphology and elemental composition of the coating surface were studied using a scanning electron microscope with a system of energy dispersive analysis (SEM/EDS, accelerating voltage is 20 kV). The composition by the coating thickness was analyzed by TOF–SIMS. To define the surface relief, we used an atomic force microscope (AFM) with a high resolution. The coating surface profile and its roughness were measured using a scanning electron microscope with a 3D laser of the VK-X100/X200 series.

The structure–phase state was analyzed on a DRON-3M diffractometer in the Cu$K\alpha$ radiation. For the monochromatization of the registered radiation, we used a graphite monochromator, which was placed in front of the detector in a secondary beam. The phase composition and structure (texture, substructure) of the coating were studied by the X-ray diffractometry analyzing the location, intensity, and shape of profiles of diffraction reflexes. The diagrams were uncoded using tables of the Powder Diffraction File international center of diffraction data.

The coating phase composition was also investigated by low-angle scattering in the Cr$K\alpha$ radiation.

A system of small circle diaphragms placed at a distance of essentially longer than the hole size allows us to approach the conditions of a plane wave with an accuracy to the r/R ratio, where r and R are diameters of diaphragms and a distance between them, respectively. The r/R value defines the size of a projection of a primary beam in the receiver plane and the smallest angle $2\theta_{min}$ (accordingly h_{min}), beginning with which one may measure the intensity of the scattered radiation, may be defined in combination with a chosen distance from a sample to a detector L. Just it is the h_{min} value that defines the small-angle resolution of this collimation system and the upper boundary (D_{max}) of sizes of inhomogeneities that may be studied on a diffractometer $D_{max} = \pi/h_{min}$.

The samples were studied by X-ray spectroscopy using a RINT-2500 V diffractometer with a position-sensitive proportional calculator (PSPC/MDGT). The operating values of the voltage and current of the X-ray diffractometer were 40 kV and 300 mA, respectively. The samples were measured at angles of 3°, 10°, and 30° in the initial state and on annealing.

For closer examination of the effect of the ion bombardment (Au ion implantation with energy of 40 keV to a dose of 10^{17} cm^2) the samples were studied at the smallest angle of the sliding drop (2θ), when the informative depth was below 100 nm.

Mechanical characteristics (hardness and elastic modulus) of the AlN$-$TiB$_2$$-$TiSi$_2$ coating were defined by nanoindentation on a Hysitron TI 950 Triboindenter device using a Berkovich indenter. To prevent the substrate effect on the hardness and elastic modulus values, indentation load was chosen so that the penetration depth did not exceed 10% of the coating thickness.

To study the irregularities on the coating surface we used a 3D Laser+Optical.

3. RESULTS AND DISCUSSION

The coatings elemental composition was examined by the X-ray fluorescent analysis both in the initial state and on the high-temperature annealing.

The presence of a high concentration of a component consisting of various light elements (C, B, O, N) in the coating stems from chemical bonds (different in type and energy) with metal atoms (Table 2).

Table 2. Elemental compositions of AlN$-$TiB$_2$$-$TiSi$_2$ coatings

Series	Annealing temperature, °C	Elemental compositions of coatings, at %						
		B	C	O	N	Al	Si	Ti
1	–	34.49	17.27	11.92	9.26	17.25	2.89	6.92
2	900	38.07	12.70	13.14	8.32	18.30	2.70	6.72
3	1300	23.57	30.36	26.84	6.97	11.45	0.32	0.49

The coating composition remains sufficiently stable at the annealing temperature 900°C and changes to the side of the saturation by oxygen and depletion in titanium atoms at the annealing temperature 1300°C.

The base of the coating is aluminum according to the metal constituent and boron according to its light filling.

The electron-microscopic studies of the topography of the coating based on the AlN$-$TiB$_2$$-$TiSi$_2$ composite ceramics (Fig. 1) showed that at the selected deposition regimes there forms an uniform structure of a protective layer with small concentrations of drop-wise fractions of micron sizes (to 10 μm in diameters). A rather even surface is observed in regions that are free of these defects of growth.

A picture in Fig. 2a demonstrates the surface morphology of the AlN$-$TiB$_2$$-$TiSi$_2$ coating produced using a 3D laser. The deposition conditions chosen experimentally allow one to develop a coating with irregularities on the surface < 1 μm (Fig. 2b), which points to a high quality of coatings deposited by magnetron sputtering of a multicomponent target. It should be noted that separate inclusions on the coating surface are the result of a local inhomogeneity of its composition. The presence of a great amount of various elements is a decisive factor in the structural state of coatings. According to the X-ray diffraction analysis (Fig. 3), in the course of the deposition there forms a coating with the amorphous-like structure. In the region of 2θ angles the X-ray pattern exhibits a halo with the maximum, while clearly defined diffraction maxima are absent. To evaluate the size of the short-range ordering region in coatings, we used the relation

$$R_m \approx 10/\Delta s, \tag{1}$$

where Δs is the width of the first wide-angle halo-like curve in the intensity$-$scattering vector coordinates, $\mathbf{s}$, (the scattering vector modulus is $s = |\mathbf{s}| = 4\pi \sin\theta/\lambda$).

Eq. (1) follows from the fact that the correlation radius (the size of the ordering region) is inversely proportional to Δs:

$$R_m = \frac{2\pi^3 z^2}{6.25\Delta s}, \tag{2}$$

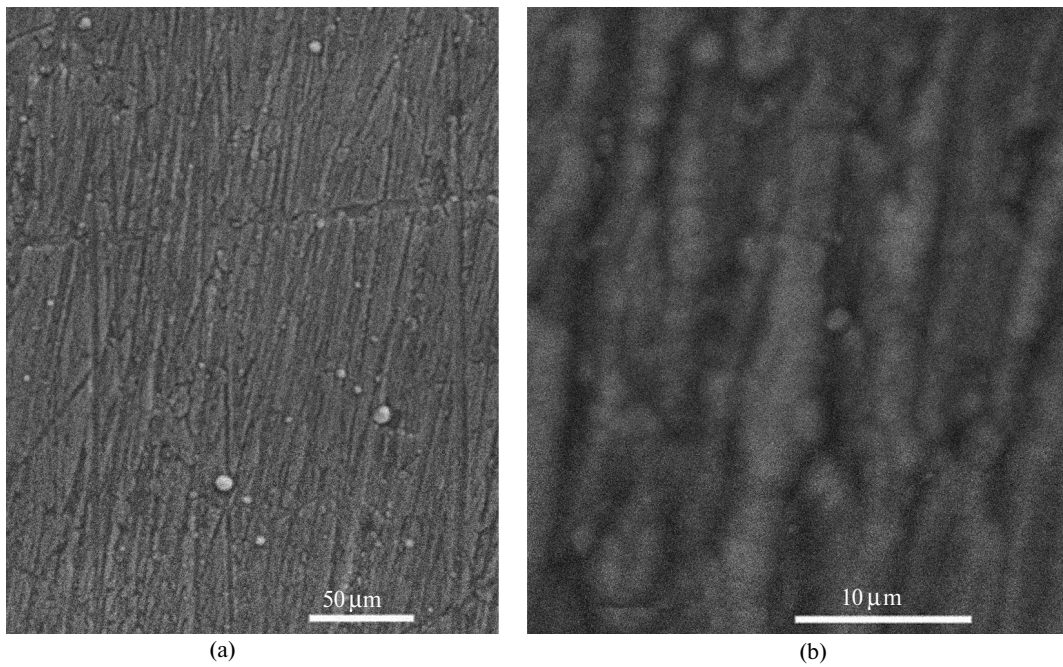where z is the index of the maximum. For the first maximum ($z = 1$) $R_m \approx 10/\Delta s$.

(a)   (b)

Fig. 1. Surface morphology of the AlN−TiB$_2$−TiSi$_2$ coating (series 1); 300× (a) and 2500× (b) magnifications.
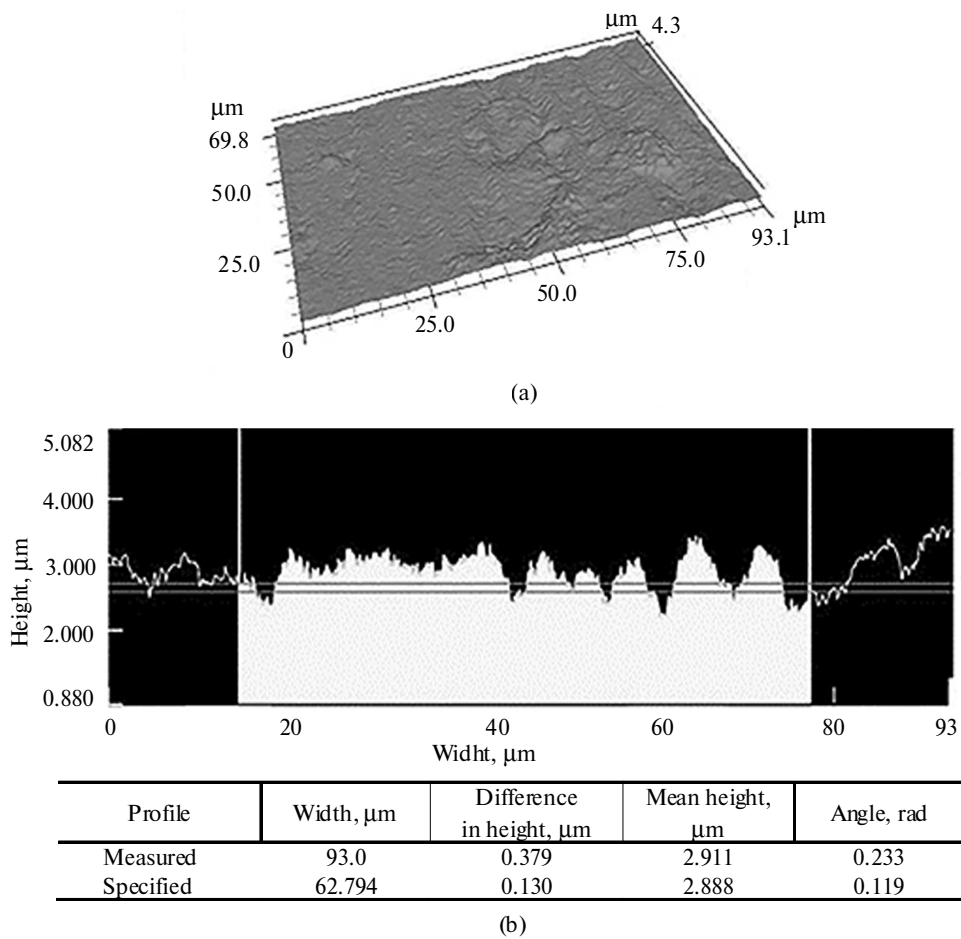

(a)

Profile	Width, μm	Difference in height, μm	Mean height, μm	Angle, rad
Measured	93.0	0.379	2.911	0.233
Specified	62.794	0.130	2.888	0.119

(b)

Fig. 2. AlN−TiB$_2$−TiSi$_2$ coating (series 1): local inhomogenities (a) profile of irregularities on the coating surface (b).
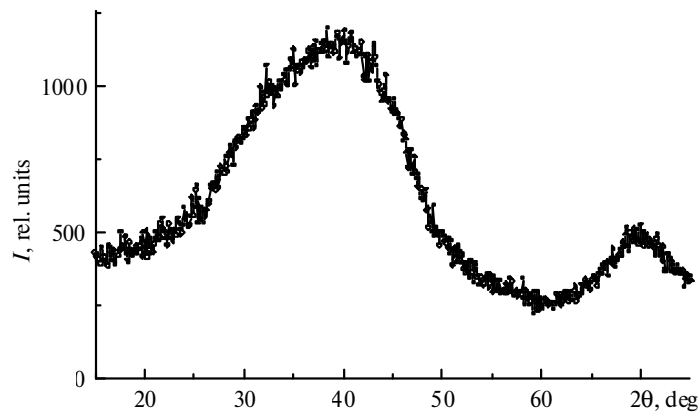
Fig. 3. Region of the diffraction pattern of an AlN−TiB$_2$−TiSi$_2$ coating produced by a pulse magnetron sputtering.

For the considered case the size of the ordering region is 10 A = 1 nm.

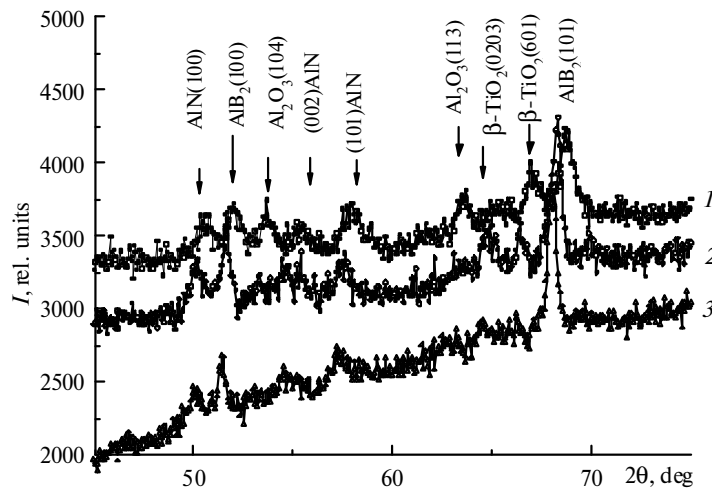X-ray diffraction spectra of samples on annealing at 900°C are given in Fig. 4.

Fig. 4. Fragments of X-ray patterns of a coating annealed at 900°C (series 2); scanning angles: 3° (*1*), 10° (*2*), 30° (*3*).

The formation of an amorphous-like structure in coatings after the deposition is an important factor responsible for their high functional properties defining high diffusion stability to external actions due to the absence of ways of easy diffusion in a material being in the amorphous state. In this case the amorphous-like structures are metastable in terms of thermodynamics and in this connection the high-temperature annealing is an important factor of their structural rearrangement.

Figure 4 shows X-ray diffraction spectra of samples annealed at the temperature 900°C. The spectra were taken by X-ray small-angle scattering. According to diffraction patterns, during the annealing the material recrystallization was activated. AlN, AlB$_2$, Al$_2$O$_3$, and β-TiO$_2$ were revealed as basic phases in the coatings composition. The phase composition correlates with the elements concentrations in a coating. Carbon in a bound state as carbide is not detected. One may suppose that carbon defined by the elemental analysis is in the form of graphite nanoinclusions, whose contribution into a diffraction picture is very small.
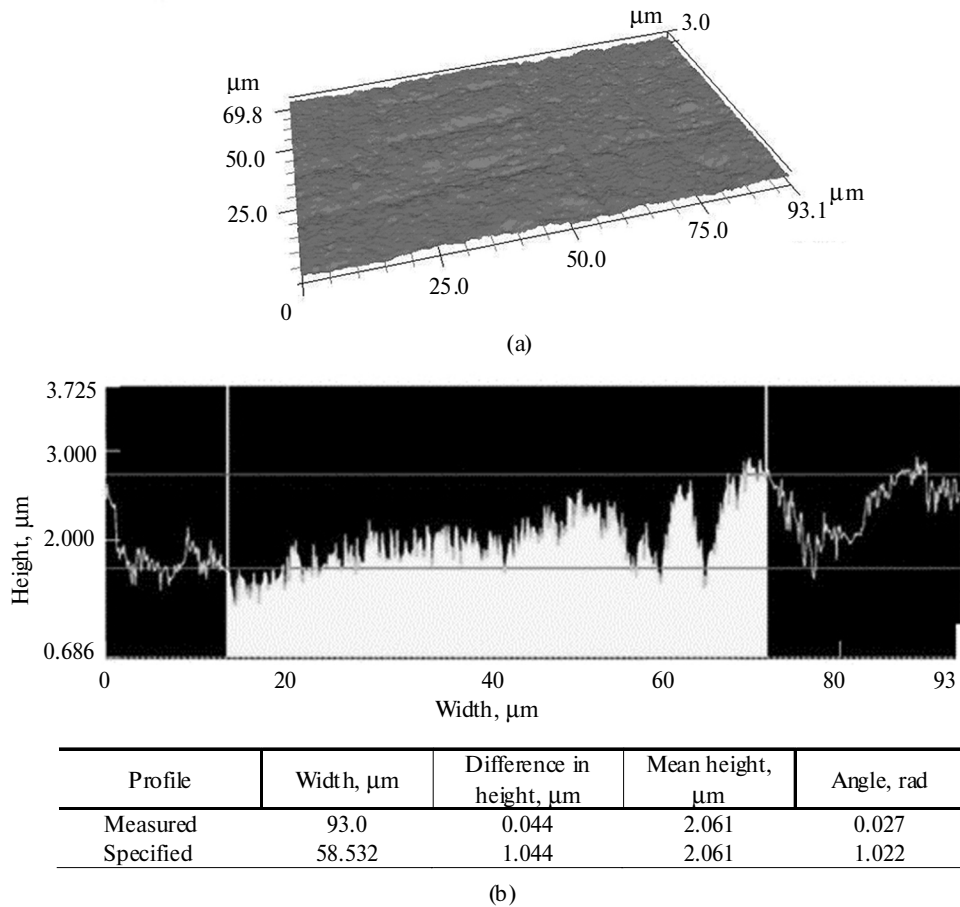
X-ray diffraction patterns taken at small angles (in a sliding geometry) showed that surface layers of the coating were enriched with oxide phases (Al$_2$O$_3$, β-TiO$_2$) and depleted of boride phases.

To deposit the coating, we choose the AlN−TiB$_2$−TiSi$_2$ composite ceramics that contained phases having melting temperatures > 1500°C. Therefore, the annealing of samples at a temperature of 900°C does not produce essential changes in the coating surface morphology (Fig. 5). It is seen in the pictures obtained at the 2500× magnification that as a result of the annealing the number of inclusions below 0.5 μm in diameter on the coating surface decreases considerably. On the backgrounds of the micron relief there forms a submicron relief represented by formations of a globule-like shape. They may be the result of the formation of titanium

and aluminum oxide phases. In the 2D image the surface exhibits a well−developed topology with a roughness exceeding 1 μm (Fig. 6).

(a)   (b)
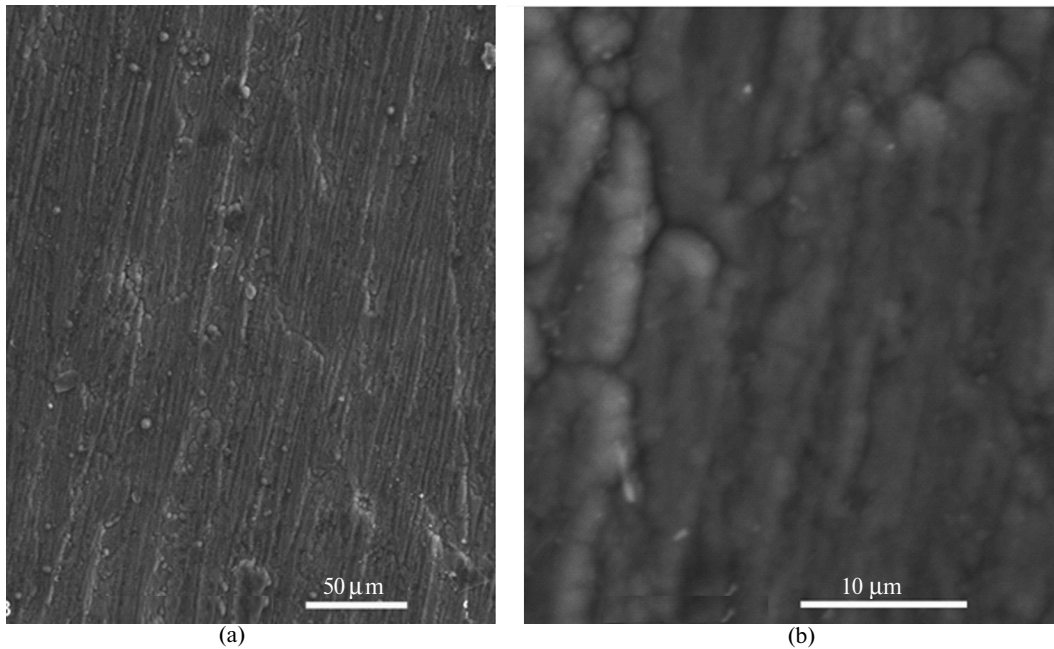
Fig. 5. Surface morphology of the coating annealed at the temperature 900°C (series 2); 300× (a) and 2500× (b) magnifications.

(a)

Profile	Width, μm	Difference in height, μm	Mean height, μm	Angle, rad
Measured	93.0	0.044	2.061	0.027
Specified	58.532	1.044	2.061	1.022

(b)

Fig. 6. $AlN-TiB_2-TiSi_2$ coating annealed at 900°C (series 2): local inhomogeneities (a), profile of irregularities on the coating surface (b).

The macrorelief formed in the annealing has a submicron subrelief of globule-like shape formations. Considering the analysis of the elemental and phase compositions of the coating surface, one may assume that these formations may be the result of the formation of oxide phases of titanium and aluminum.

The annealing at higher (1300°C) temperature brings about a fundamental change in the diffraction spectrum. The basic component of the coating becomes Al_2O_3 aluminum oxide and up to 30 vol % remains to AlB_2 (Fig. 7).
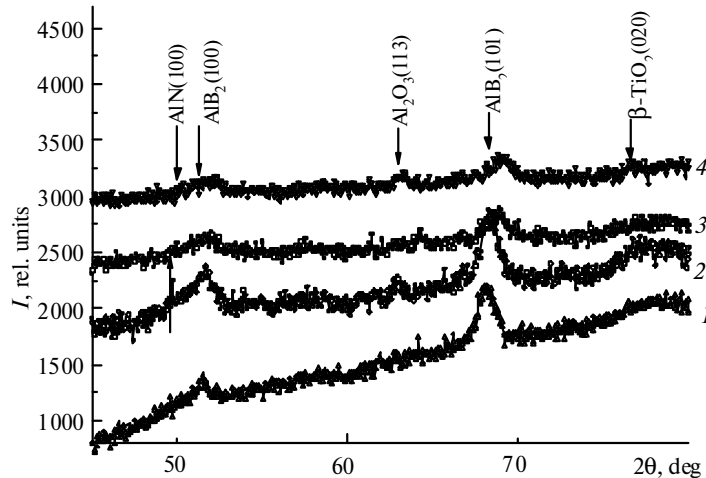

Fig. 7. Fragments of the X-ray patterns of coating taken at the inclination angles of the beam to the sample 30° (*1*), 10° (*2*), 3° (*3*) (series 3), 2° (*4*) (series 4).

The formation of Al_2O_3 and AlB_2 crystallites in this case is caused by the highest heat of the formation typical of these phases.

It should be noted that as well as in the case of the annealing at 900° the coating surface is depleted in the boride phase at the ion radiation, which stimulates further depletion of the surface in boron that manifests itself as a relative decrease of aluminum diboride peaks (Fig. 7, spectrum *4*). The decrease of the coating surface roughness, which shows up in the relatively low scatter of the background of a diffraction spectrum taken in a sliding geometry, may be assigned also to the effects of the ion implantation.

Holding samples at the temperature 1300°C activates the material recrystallization processes. The clearly defined globular substructure is absent on the surface but many various small formations appeared at the macrolevel (Fig. 8). It should be noted that they do not promote the formation of a surface with a developed relief. To the contrary, the high-temperature annealing leads to a distinct decrease of the coating surface roughness (see Figs. 2b, 6b, 9b).

To prevent the substrate effect on the hardness and elastic modulus values in measuring the hardness and elastic modulus of the (Ti, Al, Si, B)N coating on a steel substrate, the indentation loading was chosen so that the penetration depth did not exceed 10% of the coating thickness. The load−indenter penetration depth curve for the (Ti, Al, Si, B)N coating on a steel substrate is given in Fig. 10a. The maximum depth of the indenter penetration in this case was 75.5 nm.

The coating hardness was calculated from the relation

$$H = P_{max}/A, \qquad (3)$$

where P_{max} is the maximum indentation load, A is the projection area of the recovered imprint.

It is known that a high roughness of the coating surface may cause errors in the determination of an area of a sample contact with an indenter as it is indirectly found depending on the imprint depth. Nevertheless, in the present study we revealed that the coating roughness does not essentially affect the measured hardness as it makes less than 1 nm, while the radius of the Berkovich indenter is 20 μm. The measured coating hardness is 14.46 GPa at the indenter penetration depth 75.5 nm and the Young modulus is 216.71 GPa (see Fig. 10a).

The analysis of parameters of residual imprints on a coating was made by AFM (see Figs. 10b−10d). We studied the effects of pile-ups and/or sink-in of the coating material around the indenter imprint. As is seen from Fig. 10d, there is a small pile-up of the coating material around the imprint, as a result of which the real contact area turns out to be larger than the calculated one. Taking into account that the depth of the indenter

penetration is below 10% of the coating thickness, one may state that the pile-up is not caused by exceeding this threshold.

(a)   (b)
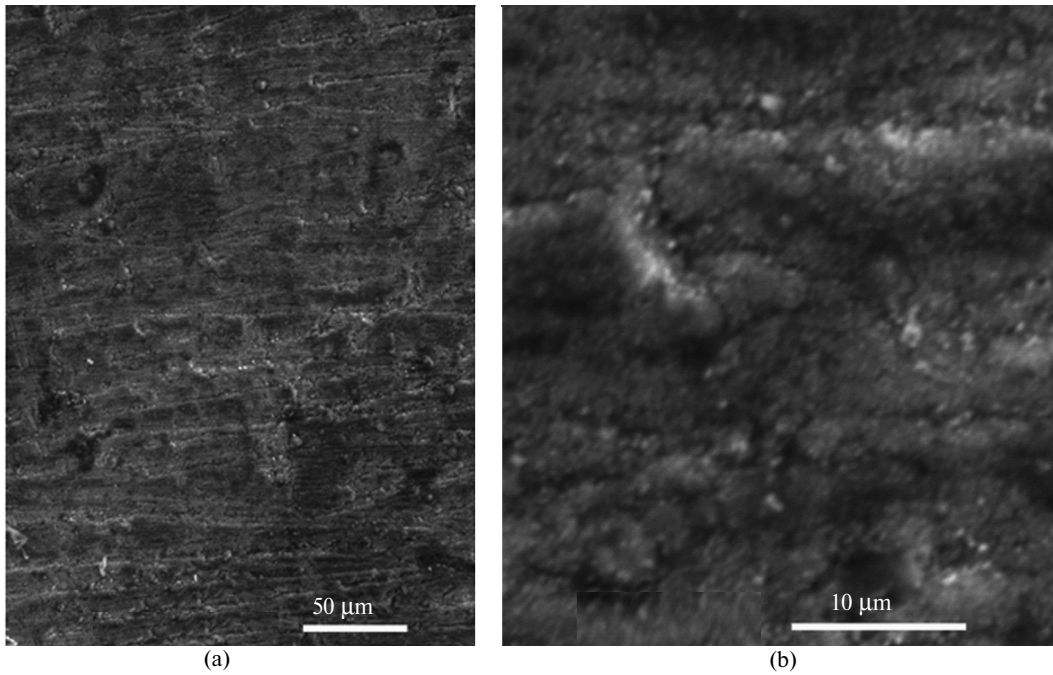
Fig. 8. Surface morphology of the AlN−TiB$_2$−SiN$_2$ coating annealed at 1300°C (series 3); 300× (a) and 2500× (b) magnifications.
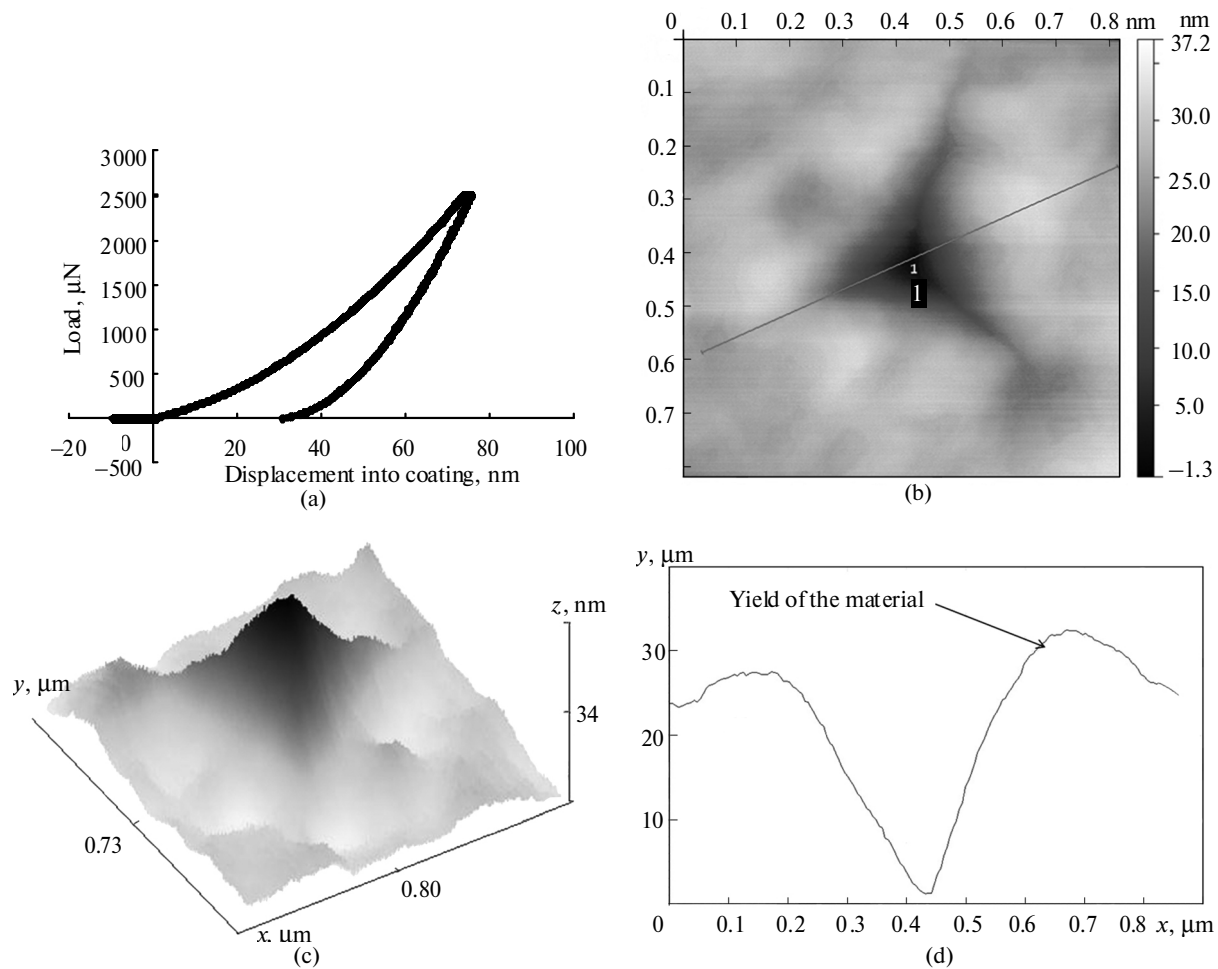

(a)

(b)
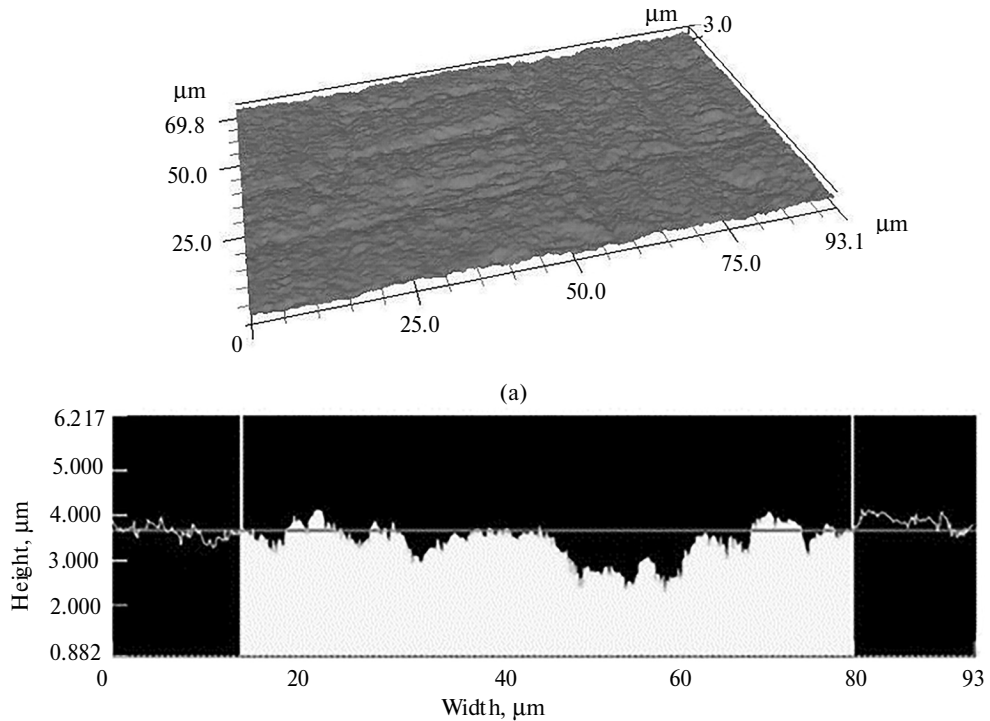
Profile	Width, μm	Difference in height, μm	Mean height, μm	Angle, rad
Measured	93.0	0.37	3.97	0.85
Specified	65.02	0.054	3.95	0.47

Fig. 9. AlN−TiB$_2$−SiN$_2$ coating annealed at 1300°C (series 3): local inhomogeneities (a), profile of irregularities on the coating surface (b).

Fig. 10. Results of the nanoindentattion of the (Ti, Al, Si, B)N coating on a steel substrate at the maximum loading 2500 μN and maximum penetration depth 75.5 nm: a load–displacement curve (a), AFM 2D image (b), AFM 3D image (c), and the cross section (d) of the residual imprint.

To define the variations of elements concentrations through the coating thickness, we used the method of the time of flying secondary mass-spectrometry (threshold of detecting is ~10^{-6} at % [21]). The use of this method allowed us to examine the coating composition in depth from the surface to the coating–substrate interface.

According to the data given in Fig. 11, one can speak with confidence about the uniformity of elements distribution in the coating depth. A long (> 7 h) bombardment by ions does not present a possibility to scatter the coating to the substrate, which is indicative of the coating great thickness (> 7 μm).

To define the hardness of a coating in different depths, we performed a dynamic nanoindentation, at which the indenter was loaded by 10 mN according to the sinusoid law. Our results indicate (Fig. 12) that at a distance of 40–80 nm from the surface (5–10% of the thickness) the coating hardness values are virtually equal (17.52–18.35 GPa). At the same time a decrease in the coating hardness is distinctly observed starting from 85 nm distance of the surface, which is the effect of a softer steel substrate.

Considering the above results of the studies we may conclude that mlticomponent coatings of the AlN–TiB_2–$TiSi_2$ system may be efficiently used to improve the performance of cutting tools in machining steels and high hardness alloys in dry cutting when high temperature occur in the cutting zone. As an example in Fig. 13 we show the results of testing for effect of cutting speed (the temperature in cutting zone is 1000–1300°C) on the tools wear rate in turning of the ShKh 15 grade hardened steel (corresponds to the AISI 52100 grade steel) [19].

As is seen, the efficiency of tools with the AlN–TiB_2–$TiSi_2$ coatings increases as the cutting speed increases. Over the range of the cutting conditions under study the use of the protective coating increases the tool wear resistance by a factor of 1.16–1.32. One may conclude that the presence of the protective coating on tools contacting surfaces leads to a change of the physical chemistry and mechanics of the contact interaction

of a workpiece and tool causing a change of the mechanism of the tool wear and increasing its operating characteristics.
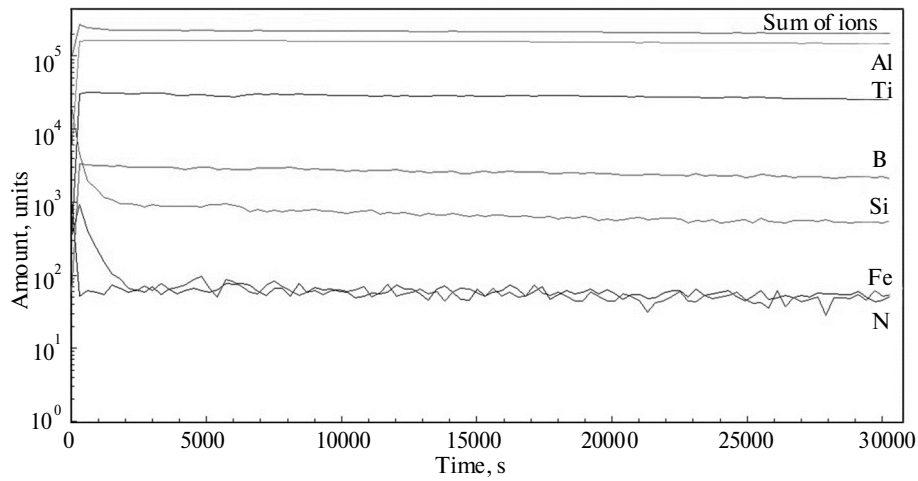

Fig. 11. Profiles of the elements concentrations in the $AlN-TiB_2-TiSi_2$ coating of series 1 in the not annealed state.
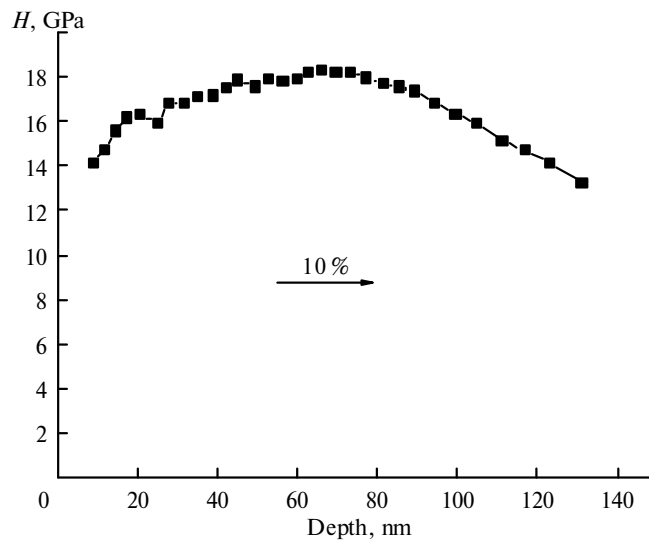

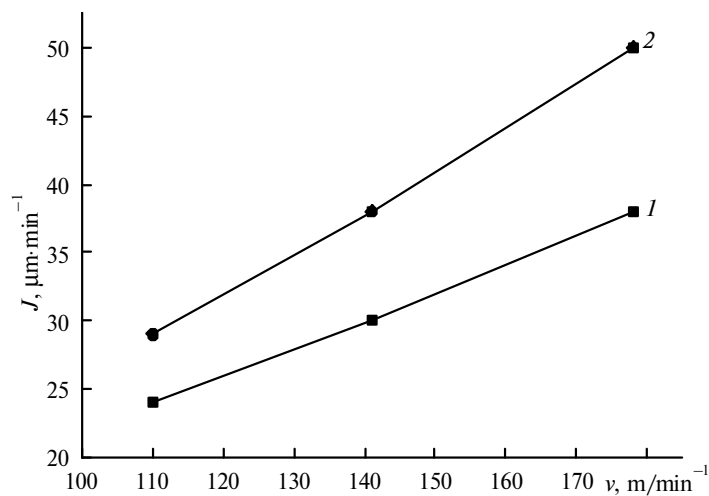**Fig. 12.** Variation of the coating hardness on a steel substrate in its depth.

Fig. 13. Effect of the cutting speed on the tool wear rate in turning ($S = 0.1$ mm/rev, $t = 0.2$ mm) ShKh15 grade (corresponds to AISI 52100) hardened steel (60 HRC): tools without a coating (*1*) and with a coating (*2*).

4. CONCLUSIONS

It has been found that in the pulse magnetron sputtering of a target having the $AlN-TiB_2-TiSi_2$ composition the formation of coatings with the amorphous-like structure takes place, which is an important factor of imparting their functional properties to the coatings specifying a high diffusion resistance to external actions due to the absence of easy diffusion ways. Since the amorphous-like structures are metastable in terms of thermodynamics, the promising direction of their structural rearrangement is high-temperature annealing.

The surface of the protective layer that have been produced by the pulse magnetron sputtering of the $AlN-TiB_2-TiSi_2$ target has a homogeneous structure with irregularities of size < 1μm.

At a high-temperature action on a coating (900 and 1300°C) its crystallization to form crystallites of size 11−25 nm is observed. It has been found that the annealing at 1300°C leads to the fundamental change in the picture of the diffraction spectrum: the basic components of the coatings become Al_2O_3 aluminum oxide and residual AlB_2 (up to 30 vol %).

It has been shown that the nanocomposite coatings of the $AlN-TiB_2-TiSi_2$ system may be used as effective protecting coatings for cutting tools, which will make it possible to increase the wear resistance of the tool at the temperature in the cutting zone to 1300°C by a factor of ~ 1.32 [19].

REFERENCES

1. Pogrebnjak, A.D. and Beresnev, V.M., *Nanocoatings Nanosystems Nanotechnologies*, Oak Park, IL, US: Bentham Science Publishers Ltd., 2012.
2. Musil, J.. Hard nanocomposite coatings: thermal stability, oxidation resistance, and toughness, *Surf. Coat. Tech.*, 2012, vol. 207, pp. 50−65.
3. Venneman, A., Stock, H.-R., Kohlscheen, J., et al., Oxidation resistance of titanium−aluminum−silicon nitride coatings, *Ibid.*, 2003, vol. 174, pp. 408−415.
4. Pogrebnjak, A.D., Shpak, A.P., Azarenkov, N.A., and Beresnev, V.M., Structures and properties of hard and superhard nanocomposite coatings, *Phys.-Usp.*, 2009, vol. 52, no. 1, pp. 29−54.
5. Veprek, S., Veprek-Heijman, M.G.J., Karvankova P., and Prochazka, J., Possible role of oxygen impurities in degradation of nc-TiN/a-Si3N4 nanocomposites, *Thin Solid Films*, 2005, vol. 23, no. 6, pp. L17−L21.
6. Pogrebnjak, A.D., Shpak, A.P., Beresnev, V.M., et al., Structure and properties of nano- and microcomposite coating based on Ti−Si−N/WC−Co−Cr, *Acta Phys. Polon. A*, 2011, vol. 120, no.1, pp. 100−104.
7. Ivashchenko, V.I., Veprek, S., Pogrebnjak, A.D., and Postolnyi, B.O., First-principles quantum molecular dynamics study of $Ti_xZr_{1x}N_{(111)}/SiN_y$ heterostructures and comparison with experimental results, *Sci. Tech. Adv. Mater.*, 2014, vol. 15, art. 025007.
8. Pogrebnjak, A.D., Ponomarev, A.G., Shpak, A.P., and Kunitskii, Yu.A., Application of micro- and nanoprobes to the analysis of small-sized 3D materials, nanosystems, and nanoobjects, *Phys.-Usp.*, vol. 55, no. 3, pp. 270−300.
9. Park, I.-W., Choi, S.R., Suh, J.H., et al., Deposition and mechanical evaluation of superhard Ti−Al−Si−N nanocomposite film by a hybrid coating system, *Thin Solid Films*, 2010, no. 3, pp. 443−448.
10. Jiang, N., Shen, Y.G., Zhang, H.J., Bao, S.N., and Hou, X.Y., Superhard nanocomposite Ti−Al−Si−N films deposited by reactive unbalanced magnetron sputtering, *Mater. Sci. Eng.,* 2006, vol. 135, no. 1, pp. 1−9.
11. Barshilia, H.C., Deepthi, B., and Rajam, K.S., Deposition and characterization of TiAlN/Si superhard nanocomposite coatings prepared by reactive direct current unbalanced magnetron sputtering, *Vacuum*, 2006, vol. 81, no. 4, pp. 479−488.
12. Söderberg, H., Odén, M., Molina-Aldareguia, J.M., and Hultman, L., Epitaxial stabilization of cubic-SiN_x in TiN/SiN_x multilayers, *Appl. Phys. Lett.*, 2005, vol. 97, no. 11, art. 114327.
13. Zhang, K., Wang, L.S., Yue, G.H., et al., Structure and mechanical properties of TiAlSiN/Si3N4 multilayer coatings, *Surf. Coat. Tech.*, 2011, vol. 205, no. 12, pp. 3588 − 3595.
14. Nguyen, T.D., Kim, S.K., and Lee, D.B., High-temperature oxidation of nano-multilayered TiAlCrSiN thin films in air, *Ibid.*, 2009, vol. 204, no. 5, pp. 697−704.
15. Fukumoto, N., Ezura, H., Yamamoto, K., et al., Effects of bilayer thickness and post-deposition annealing on the mechanical and structural properties of (Ti,Cr,Al)N/(Al,Si)N multilayer coatings, *Ibid.*, 2009, vol. 203, pp. 1343−1348.
16. Pogrebnjak, A.D., Kravchenko, Yu.A., Kislitsyn, S.B., et al., TiN/Cr/Al2O3 hybrid coatings structure features and properties from combined treatment, *Ibid.*, 2006, vol. 201, pp. 2621−2632.
17. Ning, L., Veldhuis, S.C., and Yamamoto, K., Investigation of wear behavior and chip formation for cutting tools with nano-multilayered TiAlCrN/NbN PVD coating, *Int. J. Mach. Tool Manuf.*, 2008, vol. 48, no. 6, pp. 656−665.
18. Pogrebnjak, A.D., Yakushchenko, I.V., Abadias, G., et al., The effect of the deposition parameters of nitrides of high-entropy alloys (Ti−Zr−Hf−V−Nb)N on their structure, composition, mechanical and tribological properties, *J. Superhard Mater.*, 2013, vol. 35, no. 6, pp. 356−368.

19. Beresnev, V.M., Toryanik, I.N., Sobol', O.V., et al., The use of the pulse magnetron scattering to produce coatings of the AlN−TiB$_2$−TiSi$_2$ system, *J. Techn. Phys.*, 2014, vol. 84, no. 8, pp. 118−122.
20. Grigor'eva, I.S. and Meilikhova, E.Z., *Fizicheskie velichiny: Sprav.* (Physical Magnitudes. Handbook), Moscow: Energoatomizdat, 1991.
21. Pogrebnjak, A.D., Beresnev, V.M., Demianenko, A.A., et al., Adhesive strength, superhardness, and the phase and elemental compositions of nanostructured coatings based on Ti−Hf−Si−N, *Phys. Solid State*, 2012, vol. 54, no. 9, pp. 1882−1890.

Translated by G. Kostenchuk